Research Article

Jaime A. Jiménez-Miramontes, Jorge L. Domínguez-Arvizu, Felipe A. Gaxiola-Cebreros, Blanca C. Hernández-Majalca, Juan C. Pantoja-Espinoza, Jesús M. Salinas-Gutiérrez, Virginia H. Collins-Martínez*, and Alejandro López-Ortiz

Effect of the synthesis method on the $MnCo_2O_4$ towards the photocatalytic production of H_2

https://doi.org/10.1515/rams-2022-0263
received May 25, 2022; accepted August 04, 2022

Abstract: In the present work, manganese cobaltite ($MnCo_2O_4$) spinel (MCO) was synthetized by Pechini and hydrothermal method, characterized and photocatalytically evaluated toward H_2 production through water splitting under visible-light irradiation. Characterization consisted in Thermogravimetry analysis (TGA), X-ray diffraction (XRD), X-ray photoelectron spectroscopy, scattering transmission electronic microscopy, BET surface area, UV-Vis spectroscopy, cyclic voltammetry, Hall effect, and photoluminescence. The MCO were evaluated as photocatalyst using an artificial visible light lamp and monitored by gas chromatography. XRD analysis found a pure spinel phase MCO. The surface area was ~5 $m^2 \cdot g^{-1}$ for the MCO synthetized by Pechini and increased to 155 $m^2 \cdot g^{-1}$ with the hydrothermal method with acetates as precursors. The Pechini MCO showed higher carrier mobility but the fastest recombination. Photocatalytic evaluation of the MCOs showed that the highest photocatalytic activity generated was 12 μmol H_2/g_{cat} at 8 h with the MCO obtained by hydrothermal method with the acetates.

Keywords: water splitting, spinel, manganese cobaltite, hydrogen production

*** Corresponding author: Virginia H. Collins-Martínez,**
Departamento de Ingeniería y Química de Materiales, Centro de Investigación en Materiales Avanzados, S.C., Miguel de Cervantes 120, Chihuahua, Chih., 31136, México,
e-mail: virginia.collins@cimav.edu.mx
Jaime A. Jiménez-Miramontes, Jorge L. Domínguez-Arvizu, Felipe A. Gaxiola-Cebreros, Blanca C. Hernández-Majalca, Juan C. Pantoja-Espinoza, Jesús M. Salinas-Gutiérrez, Alejandro López-Ortiz:
Departamento de Ingeniería y Química de Materiales, Centro de Investigación en Materiales Avanzados, S.C., Miguel de Cervantes 120, Chihuahua, Chih., 31136, México

1 Introduction

In recent years, the issue of energy supply has become indisputably important one of the main challenges to be overcome for humankind. With fossil fuels being the main source of energy so far, the efforts of researchers to search for environmentally friendly and sustainable alternative energies have brought about a focus on renewable energies. According to the International Energy Agency, total world primary energy consumption in 2014 was 13.7 billion tons of equivalent oil. Of this, 31.3% corresponds to oil, 28.5% to coal, 21.2% to natural gas, and the rest corresponds to renewable, nuclear, and other energies. Of the renewable energies, 72.8% corresponds to biofuels, and the remaining corresponds to energy from water, wind, tides, sun, and geothermal [1].

Another alternative that has attracted the attention of researchers is hydrogen, since it functions as an energy vector whose combustion does not generate pollutants and is highly energetic. One of the best-known processes for obtaining hydrogen is water splitting, which is a process that enables the production of hydrogen by direct water decomposition to its elements. The energy required to cleave H–O–H bonds can be supplied by different power sources: electrical (current), thermal (heat), or light (electromagnetic radiation) [2]. Energy required for the photocatalytic water splitting (1.23 eV) is provided by a semiconductor material that is able to absorb photon energy and convert it to chemical energy accompanied with a largely positive change in the Gibbs free energy through water splitting [3].

To evaluate the photocatalytic performance of materials towards the water splitting reaction, sacrificial reagents are introduced to quickly consume the photogenerated holes. For example, methanol, lactic acid, or triethanolamine, etc., is usually used as hole scavenger for H_2 production [4].

At present, this photocatalytic process has been investigated multiple times and new mechanisms, materials,

etc., have been proposed. Many metal oxide semiconductors have been studied since this reaction does not occur thermodynamically by itself, being TiO_2, the pioneer photocatalyst and to date the most used although its band gap, i.e., the difference between its conduction and valence bands, has a value of 3.2 eV, which is not active under sunlight [5]. Other materials that have shown good results are the groups of photocatalysts based on $SrTiO_3$, Zn/In/S, Ta/O, Cd/S/Zn, K/Ti/O, and Ga/Zn/O [6], but each one with advantages and disadvantages.

To improve the performance of some photocatalysts, the use of metal doping such as platinum, silver, gold, and other value metals have been reported [7–14]. This reduces the recombination of the electron–hole pair, obtaining good results in the photocatalytic activity, but in many instances a high cost in the process that is not advantageous. Chen et al. [15] reported the preparation and photocatalytic H_2 production performance of $AgNbO_3$/g-C_3N_4 composite, which showed better performance than the pure g-C_3N_4 and $AgNbO_3$. Furthermore, Chen et al. [15] fabricated $KTa_{0.75}Nb_{0.25}O_3$(KTN)/g-C_3N_4 composite through microwave heating, increasing twice the rate performance of g-C_3N_4 by adding the KTN. Zhang et al. [16] reported the use of Ag_2S to improve the performance of K-g-C_3N_4. Wang et al. [17] proposed a new preparation method for the composite Er^{3+}:$Y_3Al_5O_{12}$@Nb_2O_5 and In_2O_3 with Pt, improving the photocatalytic activity. Recently, Lv et al. [18] fabricated the photocatalyst NaY zeolite with CdS and Pt, enhancing the electron–hole separation. Chen et al. [19] showed that the photocatalytic activity of TiO_2 nanosheets increased significantly with cations doping (Na^+, K^+, Mg^+, and Al^+) and Pd.

There are some bimetallic oxide materials with properties that can be useful for the process of producing hydrogen by photocatalysis. These semiconductors are spinel-type materials that have been scarcely studied for this application. Their composition, AB_2O_4 (A and B are metal ions), can form a very extensive family containing one or more metallic elements where almost all metals, including the transitions, have been found forming these materials. Due to these multiple compositions, electronic configurations, and valence states, spinels exhibit magnetic, optical, electrical, and catalytic properties that make them suitable for various applications [20].

One of the most common spinel-type systems are Fe compounds better known as metallic ferrites, whose optical properties have shown that they can be used as photocatalysts for obtaining hydrogen through water splitting by photocatalysis [21–23]. Metal ferrites, having the general formula MFe_2O_4, are high-resistive dielectrics with great interest for their applications in high frequency drive technologies, due to their low conductivity, as well as their low current loss, compared to metal alloy films and their high saturation magnetizations and Curie temperatures. The most common examples of spinel-type ferrites are: $CuFe_2O_4$, $BaFe_2O_4$, $NiFe_2O_4$, $CoFe_2O_4$, $MgFe_2O_4$, $ZnFe_2O_4$, and $CaFe_2O_4$, where Ba, Ca, and Sr ferrites have been investigated in catalytic reactions to degrade pollutants [20,24–26] and Zn, Co, and Ba ferrites for photoelectrochemical water separation [27]. They also present the advantage of having band gap energy values suitable for being active under visible light, as well as the ability to tune the band gaps of other materials when used as supports and/or doping [28,29].

As in the case of ferrites, cobaltites can present similar features and hence obtain promising results. Cobaltites present their major application in electrochemical and electrocatalytic processes and as catalysts. Some of these cobaltites present suitable properties as catalyst in addition to a low synthesis cost, abundance, good electrical/ionic conductivity, and important redox reactions. The best known cobaltites are: $NiCo_2O_4$ [30–32], $MnCo_2O_4$ [33,34], $MgCo_2O_4$ [35,36], and $ZnCo_2O_4$ [37,38], presenting band gaps within 2–2.2 eV [30,37,39,40].

Cobaltites are spinel-like materials that have not been evaluated as photocatalysts. The main applications vary between electrochemical and electrocatalytic processes as mentioned above. In 2013, Duan et al. [33] investigated the electrochemical performance of manganese cobaltite spinel (MCO) in lithium-ion batteries. Kalubarme et al. [41] in 2015 continued this application by modifying the synthesis method to obtain a carbon-free anode. Recently, they have continued with the application of this material both as anode and as cathode in lithium-ion batteries by modifying its morphology measuring the impact this has on its performance [42–45].

This cobaltite has been tested on its use as a supercapacitor in some recent studies. In 2018, Merabet et al. [46], examined the impact on the capacitive properties of the spinel structure MCo_2O_4 by changing the metal ion M (M = Ni, Mn, Cu, and Zn). In 2017, Dong et al. [47] reported that MCO had good performance as a supercapacitor and it is still actually under study. Fan et al. [48] synthesized MCO by adding graphene with the aim of testing it as an anode in supercapacitors seeking to improve its performance and energy storage.

There is scarce information about metallic cobaltites in this application. Therefore, in the present investigation, it is intended to study the application of MCO as a photocatalyst to produce hydrogen. It has been reported

that MCO is a material whose synthesis method is not very difficult to perform so any existing method can be used.

$MnCo_2O_4$ has been synthesized in the past using several techniques such as, coprecipitation, microwave plasma, ball-milling, spray pyrolysis etc., [33]. However, the research on $MnCo_2O_4$ particles applications into different architectures and their structural development are comparatively limited because the size, morphology, composition, dispersion, and surface features of the particles have not met the needs of more advanced practical photocatalytic applications.

Moreover, the hydrothermal/solvothermal method has been widely used in the synthesis of materials because it offers important advantages over the above listed conventional techniques such as simple operation, low temperature and energy consumption, a better control of the morphology and growth control of the crystallite, uniform grain, and easy shape control. In this synthesis technique, the chemical purity of the powder materials is higher due to the crystallization processes, where growing crystals/crystallites tend to reject impurities present in the growth environment and therefore, impurities such as ions coming from metal salts or pH adjusting agents are removed from the system along with the crystallization solution [41,42]. All these features are combined to obtain high purity crystalline metal oxides with high surface area [46,48–55]. Furthermore, another simple and versatile synthesis technique is the Pechini method where the ability of certain alpha-hydroxycarboxylic acids to chelate cations and form a polymeric network when heated in a polyhydroxy alcohol solution results in a solid resin with a high homogeneous distribution that upon calcination, a ceramic with high crystallinity is obtained [52]. Pechini method is well suited to produce phase-pure powders with the desired composition and crystallite size [34] and is known for the preparation of mixed metal oxides, with certain advantages, such as low cost, homogeneous molecular or atomic mixing, stoichiometric control, low calcination temperatures, and a short time of heat treatment where the immobilization of the metal complexes in a polymeric organic network reduces the segregation of the metal particles, thus ensuring the homogeneity of the oxide [56]. Therefore, in the present research $MnCo_2O_4$ was synthesized by the modified Pechini (MCOP) [23,34,56], the Hydrothermal (MCOH) [33,57], and the modified Hydrothermal (MCOHA) [57] methods to obtain high-purity and crystalline nano-powders with high surface area at relatively low temperatures ideal for photocatalytic applications and specifically to produce very active water splitting photocatalysts for the generation of hydrogen under visible light irradiation.

2 Materials and methods

2.1 Pechini synthesis method

The material obtained by this method is denoted as MCOP. The synthesis of the MCOP by Pechini consisted in a modification of the method used in the reference literature [23,34,56]. According to the basis of Pechini method [52], citric acid (CA) and ethylene glycol (EG; Sigma-Aldrich) were used as chelating agents for the formation of the polymeric network. First, the calculated amount of EG was heated at 70°C until evaporation was noticed and then the required amount of CA was added. It was kept under constant stirring until a translucent gel-like solution was achieved and allowed to cool for 20 min at room temperature. Then, the necessary amount of $Mn(NO_3)_2{\cdot}6H_2O$ and $Co(NO_3)_2{\cdot}6H_2O$ (Sigma-Aldrich) was added, in stoichiometric ratio of 1:2, considering that spinel structure is AB_2O_4. It was kept under constant stirring at a temperature of 80°C until a gel was obtained. It was left to dry until it hardened forming a polymeric resin with the metal ions. Once dried, a thermogravimetric analysis of the organic resin was carried out to thermally decompose it and obtain the desired oxide.

2.2 Hydrothermal synthesis method

The methodology for the hydrothermal consisted in the modification of the methods used in the literature [33,58]. EG and 0.8 g NaOH as nucleating agent were used. First, stirring of 20 mL of EG was carried out at 70°C. Then, stoichiometric amounts $Mn(NO_3)_2{\cdot}6H_2O$ and $Co(NO_3)_2{\cdot}6H_2O$ were added and mixed by constant stirring with the EG. NaOH was then added dropwise. The solution was then transferred to a 40 mL Teflon autoclave and left at 120°C for 12 h. Subsequently, it was placed in a centrifuge and then the material was filtered and washed with a water-ethanol solution (1:1) several times. It was left to dry at 60°C for 5 h and finally it was exposed to a thermal treatment of 500°C for 4 h. The material obtained is denoted as MCOH.

The hydrothermal method was modified by using Mn and Co metal acetates as cation precursors, and the use of urea as reported in literature [57,59,60]. 20 mL of EG was stirred at room temperature and the calculated amounts of $Mn(CH_3COO)_2{\cdot}4H_2O$ and $Co(CH_3COO)_2{\cdot}4H_2O$ were added. It was kept under constant stirring for 20 min and then urea was added as precipitant, maintaining the stirring for another 30 min. It was then transferred to a 40 mL

Teflon autoclave, and left at 150°C for 10 h. It was then filtered and washed with water-ethanol solution. It was left to dry at 80°C for 5 h and then heat treated at 350°C for 4 h. This material is denoted as MCOHA.

3 Characterization

The material was characterized by thermogravimetry, X-ray diffraction (XRD), and spectrophotometry techniques. The value of the calcination temperature to reach the metallic cobaltite was obtained by thermal decomposition of the resin through analysis in a TGA Q500 of TA instruments, at temperatures between 25 and 980°C in air. TGA reductions were made to evaluate the presence of oxygen vacancies using 5% H_2/Ar with a flow rate of 40 mL·min^{-1} at a ramp of 10°C·min^{-1} from room temperature to 980°C. The determination of the crystalline structure through XRD analysis was performed by means of a Panalytical X'pertPRO X-ray diffractometer with copper (αCu) radiation at a step of 0.02°·s^{-1} in a range of 20–80°. X-Ray photoelectron spectroscopy (XPS) analysis was carried out using ESCALAB 250Xi Thermo Scientific spectrometer with a monochromatic Al Kα X-ray source (1486.7 eV) with a resolution of 0.45 eV. Experiments were developed with a working pressure of ~10^{-10} mbar. In the study of morphology and particle size, an analysis was performed by Field Emission Scanning Electron Microscopy (FESEM), in a JEM-2200FS equipment. The magnification used was 50–100k at 4–5 kV; for the analysis of the surface area, the nitrogen adsorption method was used at its condensation temperature (77.35 K, −195.8°C) taking 11 adsorption points in a range of 0.05–0.3 relative pressure ($p/p0$) based on the Brunauer–Emmett–Teller (BET) method in an Autosorb-1 surface characterization equipment, Quantachrome brand. To clean the surface, the sample was treated at 250°C for a minimum of 3 h under vacuum. To determine the band gap energy value, the absorption spectra by diffuse reflectance of the powders were obtained using a UV Visible Evolution 220 Thermo spectrophotometer with an integrating sphere in a range of 100–1,200 nm. The Hall effect was measured to obtain electronic properties of the materials and was carried out in Linseis L79 Hall characterization system, with a sample holder of 5 mm × 5 mm. LS 45 Fluorescence Spectrometer was used to study the photoluminescence (PL) of the samples over a wavelength range of 380–700 nm.

3.1 Electrochemical characterization

An electrochemical characterization of the material was carried out by means of Cyclic Voltammetry (CV) in a bipotentiostat model AFCBP1 Pine Instruments. The system consisted of a 3-electrode cell configuration: a 0.5 cm diameter (0.196 cm^2) glassy carbon working electrode on which the materials were deposited, a counter electrode using a 4.5 cm^2 platinum foil (9 cm^2 on both sides), and an Ag/AgCl reference electrode with KCl solution at 3 M concentration (0.210 V vs normal hydrogen electrode [NHE]). The solution used for the electrochemical cells was 0.1 M potassium ferrocyanide trihydrate ($K_4Fe(CN)_6·3H_2O$) at approximately pH 7. The solution was bubbled with nitrogen for approximately 5 min to remove possible dilute oxygen content before each measurement. Preparation of the working electrode consisted of dispersing 30 mg of the material in 80 µL of isopropanol and 0.5 µL of Nafion®, then the suspension was sonicated for a period of 10 min, and a drop of the mixture was taken and placed on the surface of the glassy carbon electrode. The isopropanol was evaporated at a temperature of 60°C for 5 min, obtaining a membrane of the material to be characterized.

3.2 Photocatalytic evaluation

The evaluation as a photocatalyst was carried out by measuring the evolution of hydrogen using the gas chromatography technique in a Clarus 500 PerkinElmer Chromatograph equipped with a thermal conductivity detector) using a specific method for measuring hydrogen and employing nitrogen as a carrier gas. The system used to carry out the separation of the water molecule consisted of a reactor with a quartz tube of 20 cm long and 4 cm in diameter with aluminum caps on the ends and an NPT sample inlet on one of them. The reactor is sealed by means of steel rods that press membranes on the ends of the tube allowing a partially leak-free seal. A magnetic stirrer, 200 mL of distilled water with 4% methanol as sacrificial reagent, and 0.2 g sample for each evaluation are placed inside the reactor. The reactor is kept in constant agitation for a period of 8 h, sampling every hour with a gas syringe while the system is irradiated by a Philips metal halide lamp of 250 W power that emits light in the visible range.

4 Results and discussion

4.1 TGA

Figure 1 shows the thermogravimetric analysis obtained from the MCO synthesized by different synthesis methods, where the thermal behavior of the material is observed. This test was used to determine the minimum calcination temperatures. Figure 1a shows the TGA obtained from the material synthesized by the Pechini method. It shows a 70% weight loss at 370°C attributed to the loss of the organics used during the synthesis: EG and CA. Figure 1b shows the behavior of the material obtained by the hydrothermal method with NaOH. In this figure, it is observed that at a temperature of 500°C there is a loss of 10% by weight, which is lower compared to the previous figure since fewer organics are used. Finally, Figure 1c shows the analysis of the material obtained by the modified hydrothermal method. In this figure, it is observed that at the temperature of 350°C, the highest loss in weight is obtained, being 40%. This loss is due to the EG, and the urea used in the method. From Figure 1 it can be observed that the loss of weight % starts at 300°C due to the elimination of water molecules and organics present in the samples. The literature presents a varied range of temperatures used to obtain the material by different synthesis methods, from 200 to 1,000°C [33,61,62]. In the case of the MCOP, different calcination temperatures were used, but at 900°C, the desired crystalline phase of the MCO was obtained (being the MCO reported in this work). In the MCOH, the temperature of 500°C was chosen according to the results presented in the TGA diagram (Figure 1b), where above this temperature no weight loss is observed meaning that a thermally stable material can be obtained. Finally, the sample synthesized by modifying the hydrothermal method (MCOHA) used a temperature of 350°C as shown in the TGA diagram in Figure 1c. Again, temperatures higher than 350°C did not present a weight change, thus obtaining a thermal stable material. For all samples, a heat treatment time of 4 h was employed.

The reduction of the calcinated MCOs was carried out by TGA using a flow with 5% H_2 in balanced Ar atmosphere to evaluate the presence of oxygen vacancies, which are related to the amount of O_2 present within each sample [21]. These vacancies are defects in the crystalline lattice and the surface of the material which play a

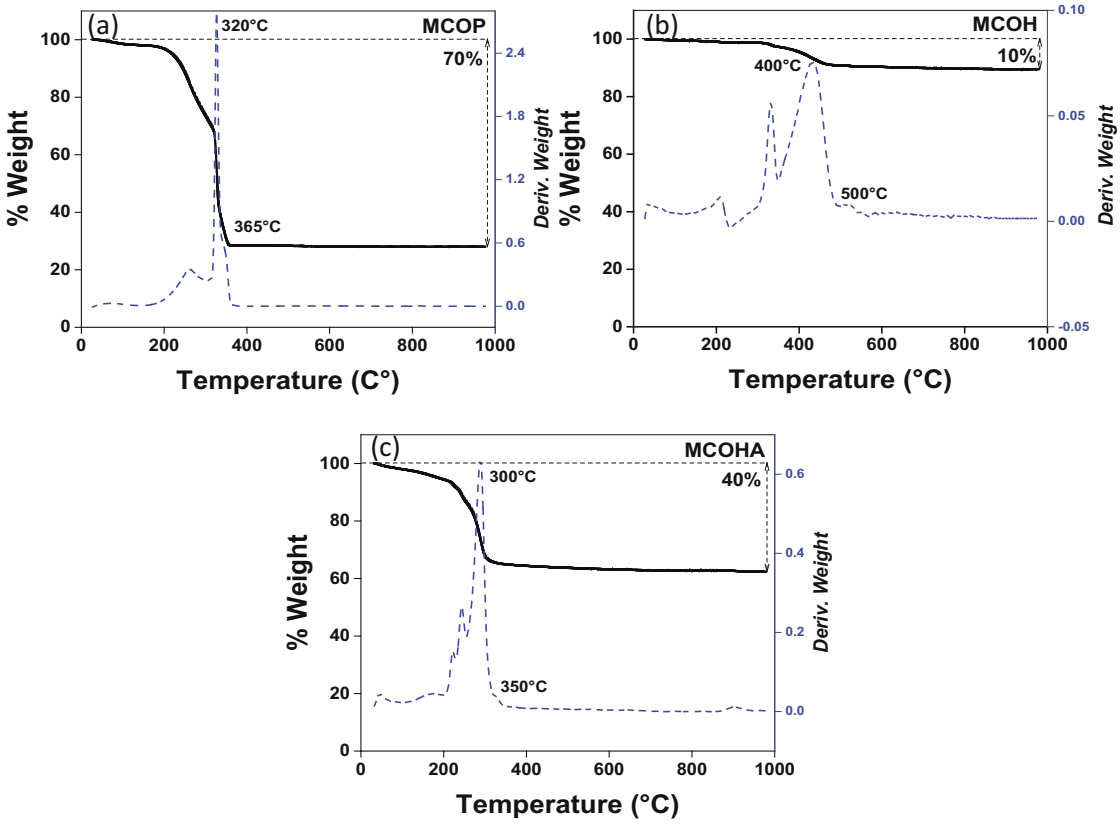

Figure 1: Thermograms of the MCO obtained by the method: (a) Pechini, (b) hydrothermal with NaOH, and (c) hydrothermal with acetates.

key role in the performance of a photocatalyst. The weight loss due to oxygen release in each MCO is shown in Figure 2. Theoretical amount of O_2 in the complete reduction of the MCO is 20%, while in the MCOP, it is about 19%, 19.5% in MCOH, and 18.4% in the MCOHA, which is slightly lesser than the others and could be associated with more oxygen vacancies.

4.2 XRD

Figure 3 shows the diffractograms obtained from the cobaltite synthesized by different methods. This figure shows the comparison of the peaks obtained with the signals of the ICDD pattern corresponding to the spinel phase MCO. The samples show the characteristic peaks at 30.56, 36.03, 37.67, 43.8, 54.39, 57.96, and 63.68° well indexed to the (220), (311), (222), (400), (422), (511), (440), and (531) crystal planes of the spinel-type $MnCo_2O_4$ (*Fd-3m*, JCPDS #00-023-1237). This indicates that the material obtained in each diffractogram coincides with the consulted card, in addition to not presenting any other signal that indicates the presence of impurities. Figure 3a shows the diffractogram obtained by the Pechini method. As mentioned above, the calcination of the MCOP

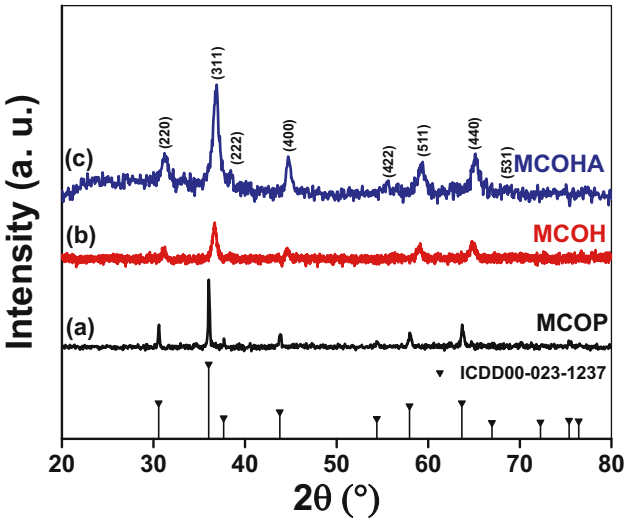

Figure 3: XRD patterns of the MCO synthetized by (a) Pechini method at 900°C, (b) hydrothermal methos with NaOH at 500°C, and (c) hydrothermal method with acetates at 350°C.

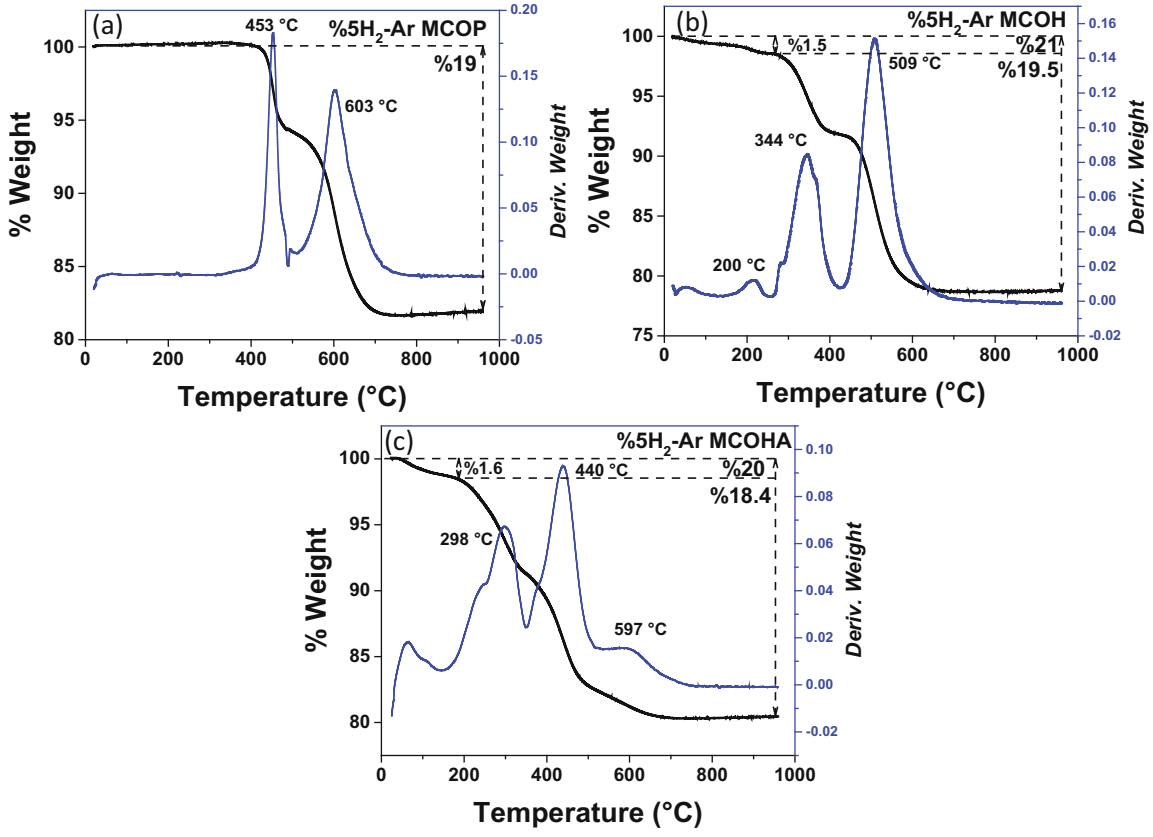

Figure 2: Thermograms of the weight loss of each MCO due to the oxygen released in the reduction with 5% H_2/Ar. (a) MCOP, (b) MCOH and (c) MCOHA.

was carried out at different temperatures, 900°C being the one that performed the best, so it is the one presented in this work. In the diffractogram, very defined and elongated peaks are observed, which indicates that it is possible to obtain a very large crystallite size, in addition to sintering, due to the high calcination temperature used. Figure 3b shows the diffraction pattern of the MCOH calcined at 500°C with peaks of lower intensity, but with a greater width than the previous ones. This indicates the possibility of obtaining small particle sizes due to smaller crystallite size than obtained in the previous MCO. The last pattern (Figure 3c) shows peaks with lower intensity and less definition than the previous ones, due to the calcination temperature of 350°C and the use of the hydrothermal method for this MCOHA. In the Figure, a shift in the peaks of the MCOH and the MCOHA can be observed. This behavior can be explained by the observations of Stangeland et al. [63] who attributed this to the incorporation of manganese into the face-centered cubic structure of spinel type.

To evaluate the impact in the crystalline structure of the MCO samples due to the temperature used in the synthesis methods, their crystallinity index (CI) was calculated using the following equation and procedure as reported in the literature [64]:

$$\mathrm{CI}\ (\%) = \frac{\mathrm{Sc}}{\mathrm{St}} \cdot 100, \tag{1}$$

where Sc represents the area of the crystalline domain and St is the area of the total domain in the diffractogram. Furthermore, the average crystallite sizes from each diffractogram were calculated with the Scherrer equation [65]. For the MCOP, the crystallinity obtained was 90% with an average crystallite size of 53 nm, as expected due to the higher temperature used. A CI of 43% and crystallite size of 20 nm was obtained for MCOH, and finally, 36% of crystallinity with crystallite size of 12 nm was obtained for MCOHA. From the above, it can be summarized that as the temperature increases, higher degrees of crystallinity are obtained but larger crystallite sizes are produced.

4.3 XPS

XPS characterization was used to determine the chemical composition and the valence state of the elements in the MCO samples. Table 1 summarizes the binding energy details of all the elements in the spectra of the MCO. As shown in Figure 4, the spectrum only represents elemental peaks of Mn, Co, and O in the three MCOs. The inevitable existence of the C peak is derived from adventitious carbon

Table 1: Summary of XPS data for the MCOs

		MCOP	MCOH	MCOHA
Co $2p_{3/2}$	Co^{2+}	781.64	781.64	781.19
	Co^{3+}	780.17	780.21	779.72
	Sat.$^{2+}_{3+}$	788.37	789.48	789.63
		785.36	785.86	784.31
Co $2p_{1/2}$	Co^{2+}	797.18	796.71	796.33
	Co^{3+}	795.50	795.22	794.82
	Sat.$^{2+}_{3+}$	805.92	804.98	805.02
		802.51	802.74	801.87
Mn $2p_{3/2}$	Mn^{2+}	641.55	641.83	641.68
	Mn^{3+}	643.46	643.73	643.88
Mn $2p_{1/2}$	Mn^{2+}	653.34	653.51	653.27
	Mn^{3+}	655.24	654.22	654.63
O 1s	M-O	530.10	530.18	529.93
	O^-/OH^-	531.29	531.79	531.09
	H_2O	532.61	533.12	532.16

species as reported in literature [42,51,66]. The peak deconvolution were carried out by a Gaussian fitting method based on the Shirley background correction with CasaXPS software [67]. In the high-resolution spectrum of Co 2p of the 3 MCO, 2 main peaks are observed at 795 and 780 eV with spin–orbit splitting of ~15 eV attributed to the multiplets Co $2p_{1/2}$ and Co $2p_{3/2}$, respectively. The evident shake up satellite peaks (denoted as "sat." in the figure), characteristic of Co^{2+} and Co^{3+} cations [66], also can be seen at ~803 and ~786 eV. Co $2p_{1/2}$ signal deconvoluted into subpeaks centered at 797 and 795 eV, while Co $2p_{3/2}$ at 782 and 780 eV approx. Subpeaks at 795.50 and 780.10 eV are ascribed to Co^{2+}, while subpeaks at 797.26 and 781.88 eV are ascribed to Co^{3+}. In XPS of Mn 2p of the MCO, 2 main peaks at 653.7 and 642 eV are observed for Mn $2p_{3/2}$ and Mn $2p_{1/2}$, respectively. These 2 signal deconvoluted into 4 subpeaks, 2 centered at 653.5 and 641.5 eV assigned to the binding energy of Mn^{2+}, and the other 2 to Mn^{3+} at 654.2 and 643.8 eV. The O 1s spectrum is often divided by 3 peaks at 530, 531, and 533 eV which belong to the lattice oxygen (metal–oxygen bond) in the spinel structure, the number of defect sites with low oxygen coordination and/or presence of hydroxyl groups and the third is atribuited to the physisorbed or chemisorbed H_2O. Using the area under the signal curve at ~531 eV of the O 1s spectre, the concentration of vacancies of the 3 MCOs were calculated as reported [68], being the MCOHA with a relative concentration of 34% oxygen vacancies, more than the others (26% MCOP and 19% MCOH) and these results are according to the reduction obtained in Section 4.1 (MCOHA > MCOP > MCOH). The peak values obtained with the XPS are agreeing to that reported in the literature [42,51,58,66,69–71]. The fitted peaks and the corresponding

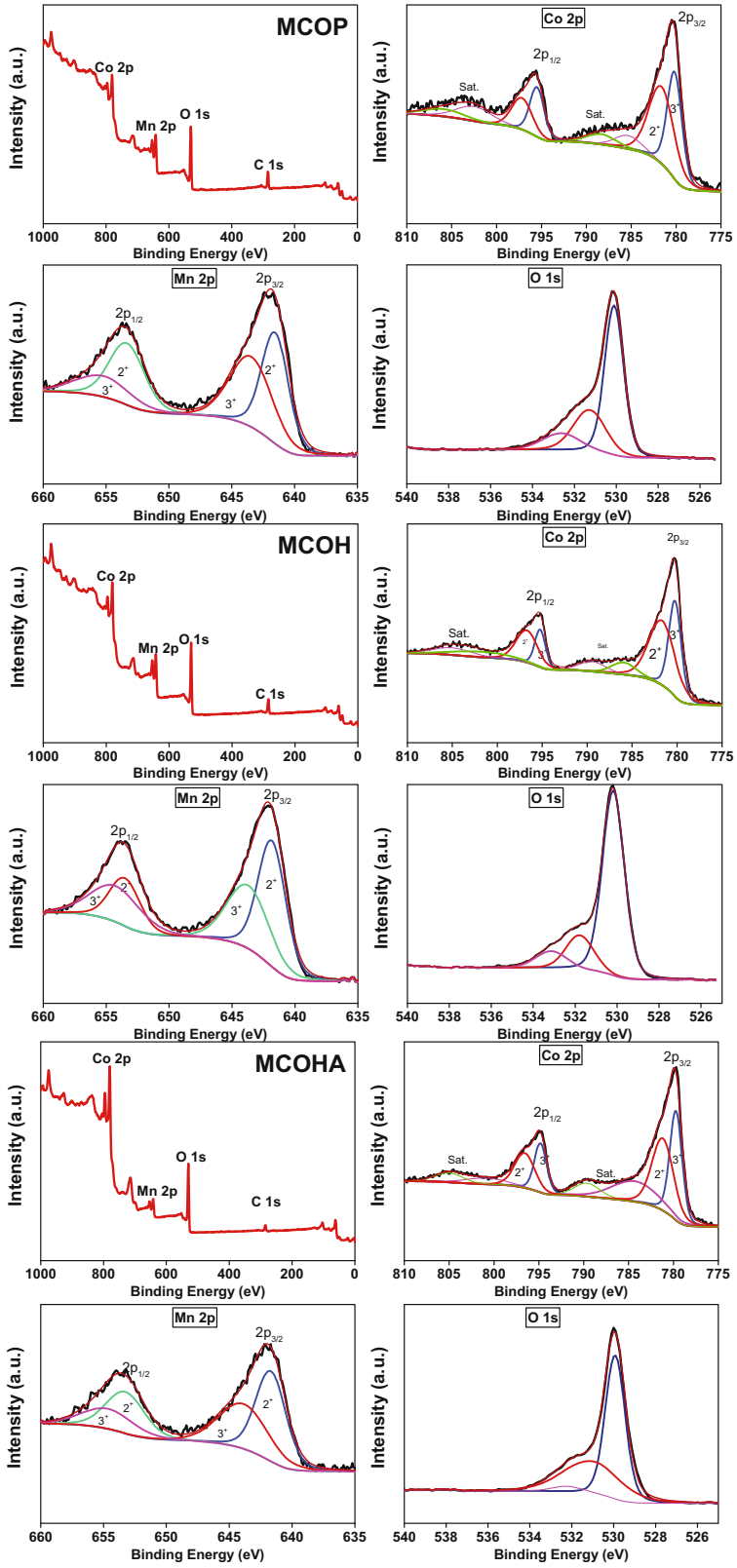

Figure 4: XPS spectra of the MCO samples: The survey spectrum and high-resolution spectra of Co 2p, Mn 2p, and O 1s.

satellites are well-indexed to the presence of Co^{2+}/Co^{3+} and Mn^{2+}/Mn^{3+} mixed valances revealing the coexistence of both states in the 3 MCOs. XPS also allow us to determinate the cation distribution between octahedral and tetrahedral sites to determinate the type of spinel-cobaltite obtained. If a normal spinel is formed, all the Co^{3+} ions occupy octahedral sites, and all the Mn^{2+} ions occupy tetrahedral sites. For an inverse spinel, half of the Co^{3+} ions are occupying the octahedral sites (Oh), and the other half occupies the tetrahedral sites (Th) along with all the Mn^{2+} ions. In 2015, Aghavnian et al. [72] and Rodríguez-Rodríguez et al. [73] in 2019, calculated these sites with the fitting of the peaks Co $2p_{3/2}$ and Mn $2p_{3/2}$ since it is more precise due to their higher intensity signal than the $2p_{1/2}$. The resulting fitting gives the proportion of the Oh and the Th sites occupied by the cations. The Co(Oh) obtained was 53.04% for MCOP, 68.61% for MCOH, and 47.64% for MCOHA, hence almost half of the Co^{3+} are in octahedral sites and therefore the spinel obtained is an inversal spinel type.

4.4 Scattering transmission electron microscopy (STEM)

Figure 5 presents the images obtained by STEM of the MCO synthesized by the different synthesis methods with a unimodal particle size distribution. In the upper part (Figure 5a) the MCOP is shown, being evident the degree of sintering present in the particles due to the 900°C temperature used for calcination. The morphology is also affected, observing particles with irregular polygon shape and mode values with size of 478 nm. Figure 5b shows the MCOH. In this image, irregular particles with mode size of 30 nm are observed, much smaller compared to the MCOP; this is attributed to the hydrothermal method with the NAOH since it allows to have a better control in the particle size in addition to a lower use of calcination temperature [53,54]. This is also the case in Figure 5c, where MCOHA is observed with a mode particle size of 10 nm with irregular morphology. This size can be attributed to the modification

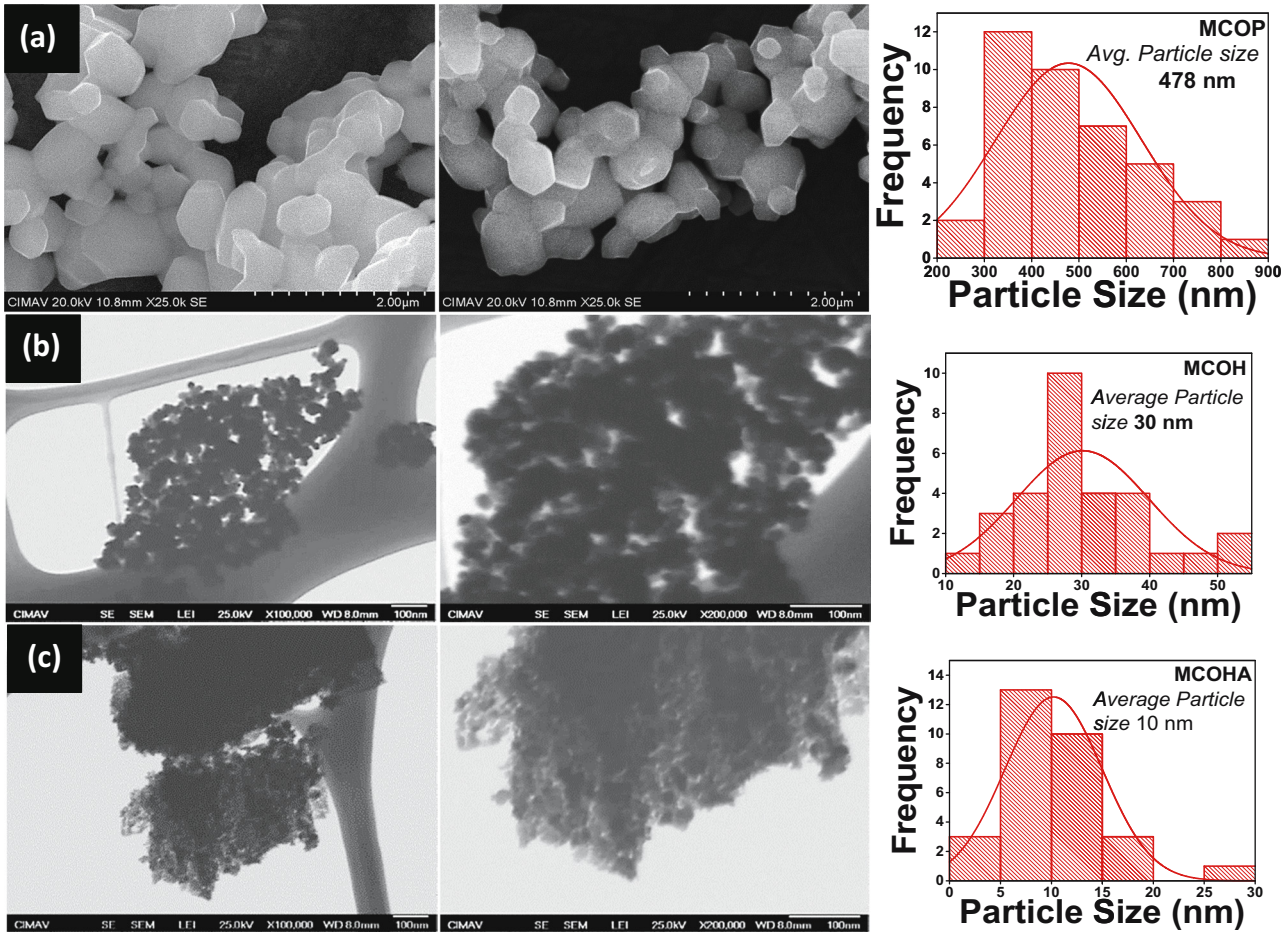

Figure 5: STEM images of the MCO synthetized by different methods: (a) pechini at 900°C, (b) hydrothermal with NaOH at 500°C, and (c) hydrothermal with acetates at 350°C.

of the hydrothermal method by using acetates as precursors favoring an increase in surface area and small particle size as mentioned by Kurajica et al. [60]. The size obtained in MCOHA is much smaller compared to MCOP and MCOH, even after using the same synthesis method. The results of the particle size were according to the expected crystallite size obtained in Section 4.2, since the temperature used was higher, the obtained particle size was larger.

4.5 BET area surface

For the analysis of the surface area, the BET method [74] was used, obtaining the nitrogen adsorption–desorption isotherms in the MCO shown in Figure 6. In the case of MCOP and MCOH, isotherms show a normal behavior on the physisorption, and a significant presence of hysteresis loop is not observed, therefore the surface area obtained in these two is attributed only to the particles. In the MCOHA isotherm, where this loop is observed, this type is classified as type IV according to IUPAC [75]. This is characteristic of a presumably mesoporous material, hence the MCOHA obtained is mesoporous, which is possible as reported by Li et al. [57], where the cobaltite obtained by hydrothermal using nitrates showed mesoporosity. Furthermore, there are reports of other cobaltites presenting the same hysteresis behavior [76–78].

Table 2 shows the surface area values obtained from the analysis of the isotherms, which vary from 5 to 155 $m^2 \cdot g^{-1}$. This remarkable change in the areas is due to the temperatures and the method used in each synthesis, since in the MCOP the 900°C temperature had a great impact on both the particle size and the surface area of the material, while in the hydrothermal method, better results were obtained with lower temperatures. Li et al. [59] reported having obtained an area of 80 $m^2 \cdot g^{-1}$ and reported that it is higher than those found in other MCO materials, but this value is lower than that obtained in the MCOHA in this work. Table 2 shows this comparison.

4.6 UV-Vis spectroscopy

A UV-Vis spectroscopy analysis was performed on the powders to determine the region of the light spectrum

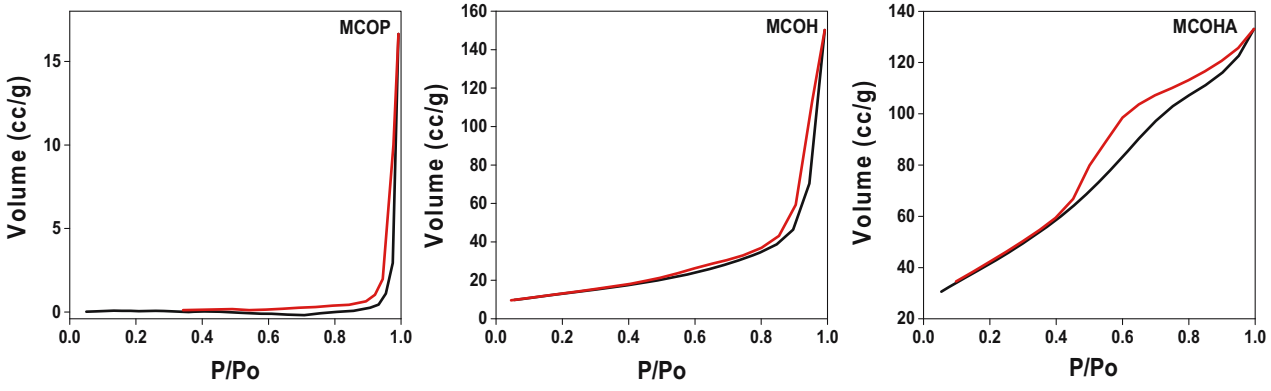

Figure 6: BET isotherms of the MCO synthetized by the method: (left) Pechini at 900°C, (middle) hydrothermal with NaOH at 500°C, and (right) Hydrothermal with acetates at 350°C.

Table 2: BET surface area comparison between MCO synthetized in this work against the reported literature values

Compound	Synthesis method	Temperature (°C)	Calcinationtime (h)	A ($m^2 \cdot g^{-1}$)	Reference
MCOP	Pechini	900	4	5	This work
MCOH	Hydrothermal	500	4	58	This work
MCOHA	Hydrothermal	350	4	155	This work
$MnCo_2O_4$	Hydrothermal	600	4	80	[59]
$MnCo_2O_4$	Combustion and hydrothermal	400	4	20 and 47	[75]
$MnCo_2O_4$	Hydrothermal	300 and 400	6	50 and 28	[79]

absorbed by the materials. From the diffuse reflectance spectra, the band gap of each material was determined employing the Kubelka–Munk method. By means of the reflectance R obtained from each phase and substituted into the Kubelka–Munk equation (2) [3,80]:

$$f(R) = \frac{(1-R)^2}{2R} \approx \alpha. \quad (2)$$

Then, using the Tauc relation: $(\alpha h\nu)^n$ vs E, the plots in Figure 7 were obtained. For semiconductors with direct band gap, $n = 2$ and for indirect, $n = 1/2$. In the graphs, a tangent line is drawn at the point with the steepest slope of the graph extending to the x-axis estimating the band gap in eV [3]. In these Tauc plots the band gap of each MCO was estimated, obtaining an approximate value of 1.30 eV in all three. Table 3 shows the comparison of the band gap of each of the MCOs with what is reported in the literature. The table shows that the values obtained in this work are different from those reported in the literature, but even among the same authors there is a difference in the values. Therefore, a characterization by CV was performed in order to verify the values obtained in this work.

Table 3: Band gap comparison of the MCO synthetized in this work against the reported values in the literature

Compound	Synthesis method	eV	Reference
MCOP	Pechini	1.30	This work
MCOH	Hydrothermal	1.31	This work
MCOHA	Hydrothermal	1.31	This work
$MnCo_2O_4$	Chloride synthesis	2.1	[39]
$MnCo_2O_4$	Hydrothermal	1.69	[51]
$MnCo_2O_4$	Co-precipitation	1.2	[81]
$MnCo_2O_4$	Sol–gel citrate	4.9	[82]

4.7 CV

Since the band gap value obtained is just the necessary potential, it is important to determine that the CB level of

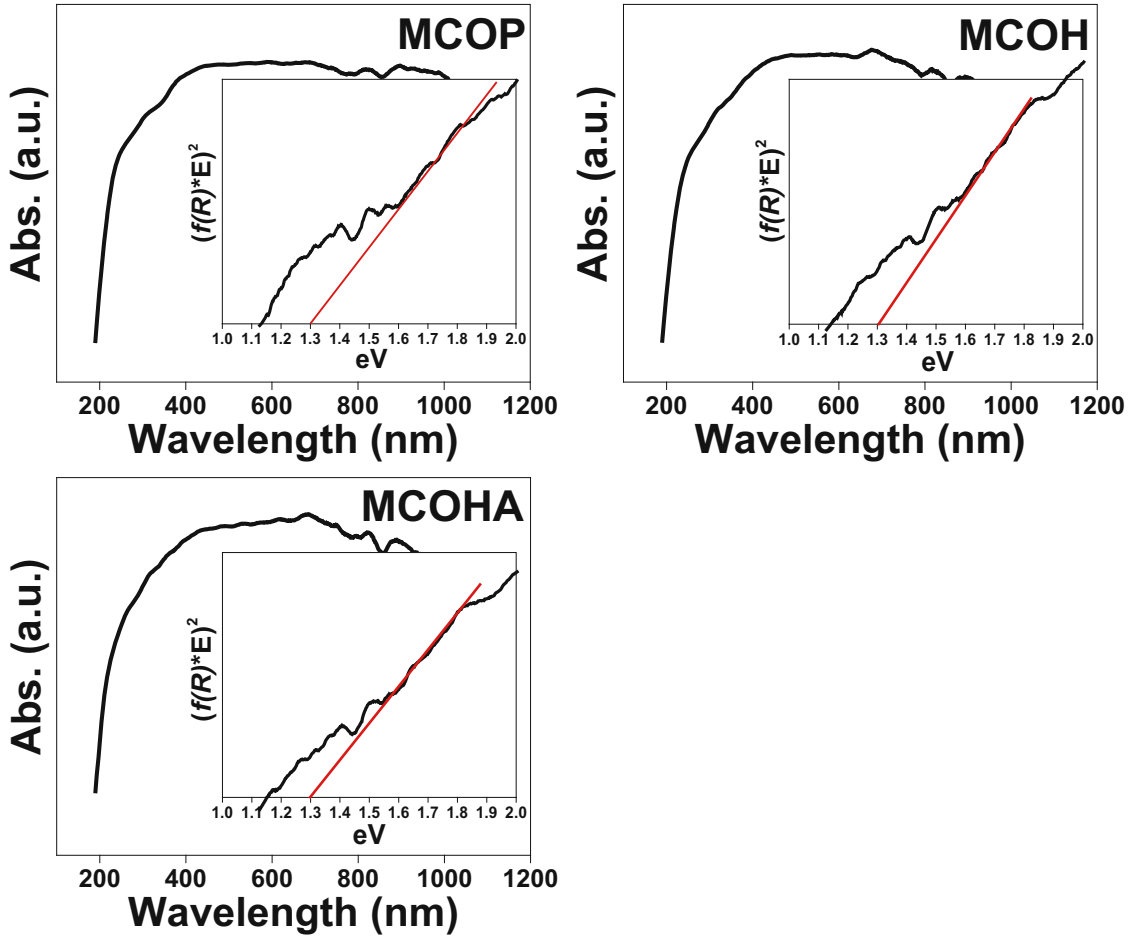

Figure 7: Absorption spectra and Tauc plots for the estimation of the direct band gap for the MCOP, MCOH, and MCOHA.

the photocatalyst is sufficiently negative compared to the H^+/H_2 redox potential. Therefore, an electrochemical characterization of each MCO was performed by CV. The electrochemical data obtained from the voltammetry plots is very valuable information since it allows to have a relative estimation of the position of the redox potentials of the material. These values in turn are approximations to the ionization potential of the material between its valence and conduction bands [83–85]. The voltammograms of the synthesized MCO are shown in Figure 8. In the −0.5 V potential region is the reduction potential of each of the MCOs. The value is very similar in all, being slightly different only by the synthesis method, stoichiometry, doping, etc., as mentioned in the literature [86]. Table 4 shows the data of each of the MCO compared with the optical band gap calculated in this work and with that reported by Zheng and Lei [51]. They report the characterization obtained by the Mott–Schottky method, which, although it is not the same characterization method used, also makes use of the basic principles of electrochemistry so the values are very close [87]. The table also shows the correction of the potential values obtained, since these values were obtained against the Ag/AgCl electrode, and it is necessary to convert them against the NHE to know if it is sufficiently negative.

According to the electrochemical analysis, the synthesized MCOs presented an approximate negative reduction potential value of −0.3 eV, higher than the H^+/H_2 redox potential. Based on these results, it is possible to draw a representation of the photogenerated charge carriers of the MCOs and this is presented in Figure 9. Here it can be observed that this value (−0.3 eV) is barely sufficient since, when calculating the electrochemical band gap of each one, a value within the range of 1.44 eV is achieved. By comparing this value against the needed 1.23 eV and considering that it has been previously reported that it is required to reach a value of 1.6 eV to be able to perform the photocatalytic phenomenon without problems, this value may become an obstacle to obtain a good performance of the photocatalyst in the production of hydrogen. According to the research carried out by Admassie et al. [88], the values obtained for the electrochemical gap and the optical gap can differ by ±0.15 eV, generally with the optical gap being slightly smaller. This, according to Inamdar et al. [89], is due to the Coulombic interaction of the electron–hole pair, i.e., slightly more energy is

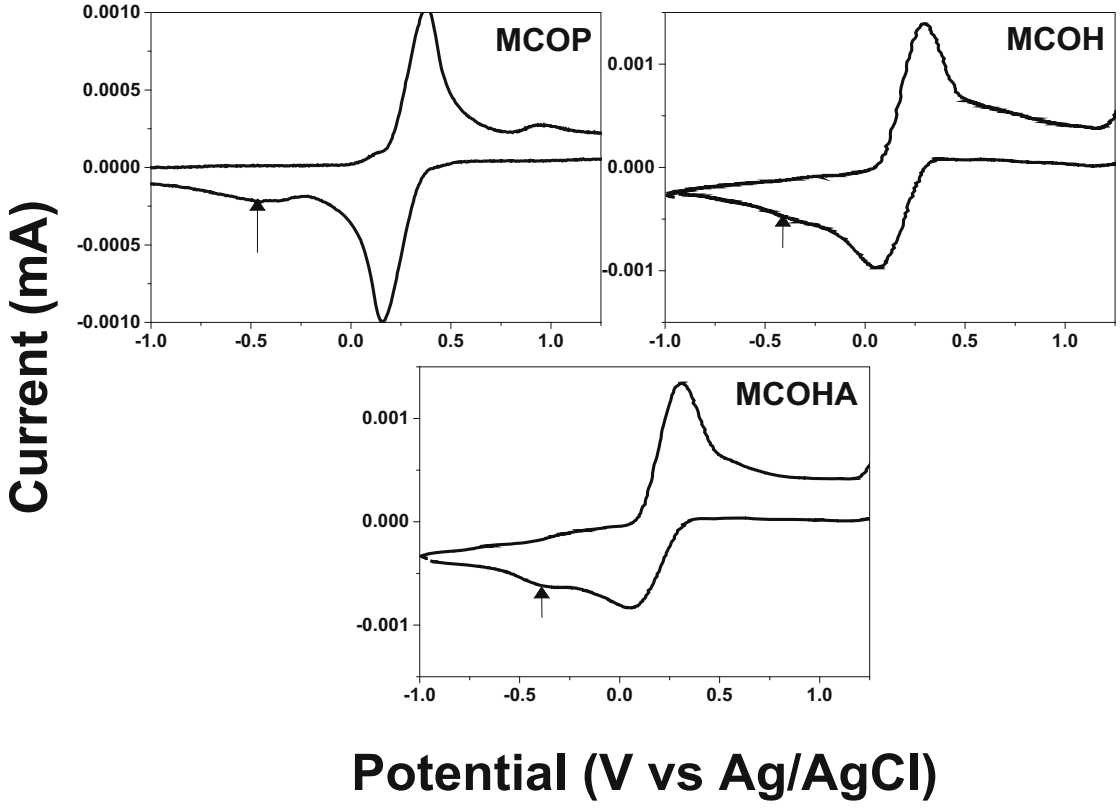

Figure 8: Voltammograms of the MCO synthetized by the methods: (top left) Pechini, (top right) hydrothermal with NaOH, and (bottom) hydrothermal with acetates.

Table 4: Values obtained from the voltammograms

Compound	Reduction potential	Literature	Oxidation potential	Adjustment 0.205 V		Electrochem. Bg. eV	Optic. Bg. eV
MCOP	−0.52	−0.69 V [51]	0.97	−0.315	1.175	1.49	1.30
MCOH	−0.48		0.96	−0.275	1.165	1.44	1.30
MCOHA	−0.47		0.96	−0.265	1.165	1.43	1.31

required in the redox process than in the excitation of charge carriers from the conduction band to the valence band.

4.8 Hall effect

To obtain two of the main electrical properties from synthesized MCOs such as mobility and charge carrier concentration (CCC), the Hall effect with the configuration of Van de Pauw [90] was measured obtaining the results as shown in Table 5. From this table, the MCOP presented a CCC of -2.6×10^{16} cm^{-3} with the highest mobility of -48.6 cm^2·V^{-1}·s^{-1}. MCOH shows a CCC of -4.2×10^{16} cm^{-3} with -25.9 cm^2·V^{-1}·s^{-1}. Finally, the MCOHA shows better CCC with -13.0×10^{16} cm^{-3} and a mobility of -3.7 cm^2·V^{-1}·s^{-1}. On one hand, the Hall effect measurements showed that samples belong to a n-type conductive nature, as reported in the literature [91]. On the other hand, results from CCC indicate that MCOP and MCOH exhibit a similar behavior between $3–4 \times 10^{16}$ cm^{-3}. Whereas MCOHA shows a higher CCC in the order of magnitude which can be attributed to the greater amount of oxygen vacancies, as mentioned previously in the XPS section and in agreement with that reported by Selim et al. [92], who associated the increase in CCC with a higher concentration of oxygen vacancies present in the material.

The order of the materials in terms of mobility is as follows: MCOP > MCOH > MCOHA. This order is presumably related to the crystallinity index as reported in the XRD section. The higher crystallinity of MCOP result in higher mobility, agreeing to that reported in the literature that charge typically moves faster in crystalline regions [93]. In the case of the MCOH, its crystallinity is slightly higher than the MCOHA, obtaining greater mobility than this last one, but with less CCC.

Since there is scarce knowledge about these properties of the MCO, the obtained results provide new information for these types of materials, which can be used in further investigations.

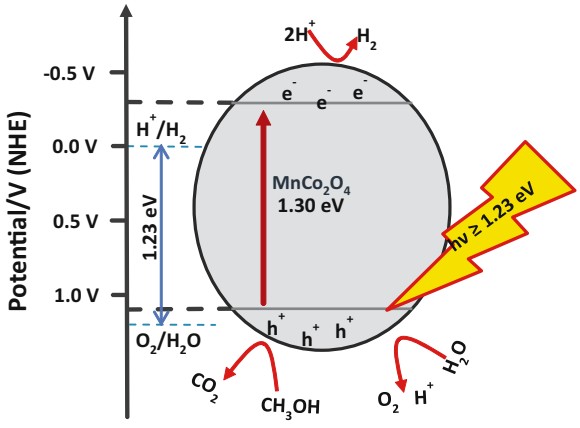

Figure 9: Schematic of the photogenerated charge carriers of the MCOs for the visible-light photocatalytic H_2 production from H_2O.

4.9 Charge separation efficiency

The method of the PL spectroscopy is a common technique used to study the separation efficiency of the photogenerated charge carriers, as well as their migration and transference in a photocatalyst [91]. Figure 10 represents the PL spectra of the MCOP, MCOH, and MCOHA. In this figure is evident a strong PL signal for the three samples when are excited by a wavelength of 470 nm, suggesting that the higher the intensity of the peak the faster the annihilation of the photoexcited electron–hole pairs as reported in the literature [15,16,94].

In general, a low PL intensity shows a better efficiency of charge separation. Likewise, these efficiencies can be directly related to the CCC [95] and as stated before this is due to the oxygen vacancies of the materials that hinder charge carrier recombination. Analysis of PL results indicate that the most efficient charge separation

Table 5: Electrical properties of the MCO samples

Compound	CCC (cm^{-3})	Mobility (cm^2·V^{-1}·s^{-1})
MCOP	-2.6×10^{16}	−48.6
MCOH	-4.2×10^{16}	−25.9
MCOHA	-13.0×10^{16}	−3.7

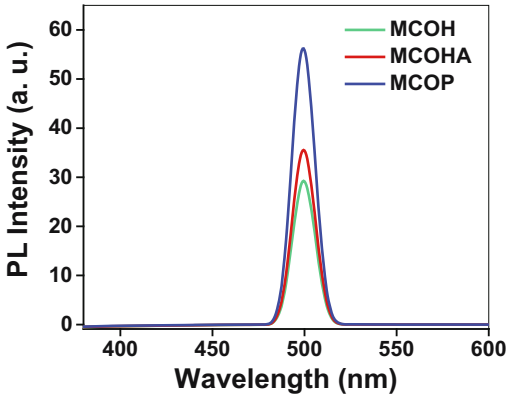

Figure 10: PL spectra of the MCO samples.

is presented by MCOH with the highest CCC, followed closely by MCOHA, and the least efficient with the lowest CCC is shown by MCOP.

4.10 Hydrogen production

Figure 11 shows the monitoring of the photocatalytic hydrogen production by evaluating the different MCOs, in a total time of 8 h. According to the figure, the MCOHA is the one that shows the best performance as a photocatalyst at the end of the evaluation time. Table 6 shows the results obtained in the evaluation of the materials as photocatalysts. The MCOP presented a production of 9,200 nmol of H_2/g_{cat}, the MCOH of 5,074 nmol of H_2/g_{cat} and, finally, the MCOHA with a production of 12,050 nmol of H_2/g_{cat}. As mentioned in Section 2.1, the first synthesis method used to obtain the MCO was the Pechini method, and it was found that calcination at 900°C resulted in the

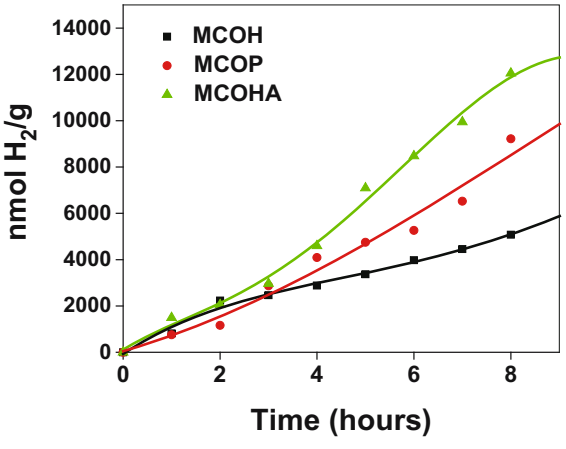

Figure 11: Photocatalytic evaluation of the MCOs synthetized for the hydrogen production.

Table 6: Performance of the MCO synthesized by different methods

Compound	A ($m^2 \cdot g^{-1}$)	nmol H_2/g_{cat} in 8 h	nmol $H_2 \cdot (g_{cat} \cdot h^{-1})$
MCOP	5	9,200	1,150
MCOH	58	5,074	634
MCOHA	155	12,050	1,506

best production, sacrificing a good surface area and particle size (5 $m^2 \cdot g^{-1}$ and 500 nm). Later, the hydrothermal method with the use of NaOH allowed improving these properties, since the excess of OH^- accelerates nucleation and the EG control the growth [33] obtaining an increase in surface area and small particle size (58 $m^2 \cdot g^{-1}$ and 40 nm), affecting hydrogen production. By modifying the hydrothermal method using acetates, urea, and EG as precursors, it was possible to obtain smaller particle sizes and increase the surface area significantly, due to the fact that the formation of a metal alkoxide is favored and when it decomposes it forms the desired oxide with very high areas with the possibility of larger active sites [59,60,96]. In addition, a better photocatalytic performance was obtained in terms of time with the MCOHA but when comparing the production in terms of surface area, MCOP is positioned as the best. This is due to the fact that a higher temperature favors higher crystallinity; higher crystallinity leads to a decrease in defects, as vacancies of oxygen, which in turn improve the recombination between charge carriers [3,39]. In the XPS analysis of O 1s shown in Section 4.3, the MCOHA have 34% oxygen vacancies, more than the MCOP, and these vacancies can act as doping elements introducing defect and preventing recombination, one of the main obstacles in photocatalysis [97,98]. The high calcination temperature (900°C) of the MCOP results in better crystalline quality but specific surface area lower than the MCOHA (350°C): 90% crystalline with 5 $m^2 \cdot g^{-1}$ vs 36% and 155 $m^2 \cdot g^{-1}$, respectively. This result leads to high surface area and more active sites and therefore a better performance, even with the disadvantage of possible defects. If the calcination temperature is high, the crystalline quality is good, but the specific surface area is low and could result in poor photocatalytic activity due to the lack of active sites for hydrogen evolution [9], so it is important to get a balance between these properties to obtain a good photocatalyst. Also, PL and Hall Effect measurements confirmed findings discussed above. These results showed that the MCOP presented the highest mobility and fastest recombination of the charge carriers, possibly due to its high crystallinity, but with the lowest CCC, which influence in its intermediate photocatalytic performance. Whereas the properties of MCOHA are superior, since its highest CCC, slowest

recombination, and high surface allow more photocatalytic interaction with the water molecules; even with the lowest mobility, its photocatalytic performance was the best.

The MCOHA was the sample with highest evolution rate of 1.506 $\mu mol \cdot g \cdot h^{-1}$, but when compared with the 730 $\mu mol \cdot g \cdot h^{-1}$ of $SrFe_2O_4$ reported by our group [23], the result is not as promising as expected. Recently, heterojunctions and precious metals as dopants were used to improve the performance of the photocatalyst as reported by Fang et al. [10], enhancing the rate 2.7 times of the pure g-C_3N_4 preparing the Pt/g-C_3N_4/BiOBr photocatalyst (361 $\mu mol \cdot g^{-1} \cdot h^{-1}$). Lv et al. [18] using the NaY zeolite with Cds and Pt, showed a H_2 production rate of 686.5 $\mu mol \cdot g^{-1} \cdot h^{-1}$. Yet, the development of TiO_2 remains under investigation as reported recently by Chen et al. [19] in 2022, loading Pd nanoparticles and doping ions in TiO_2 nanosheets, obtaining 76.6 $\mu mol \cdot g^{-1} \cdot h^{-1}$ with Pd/0.2% K^+ -TiO_2.

Although it was possible to improve the properties of the material without affecting its performance, the production obtained is low compared to that reported in the literature. This may be mainly since the band gap of 1.3 eV and reduction potential (−0.3 eV) presented by the material are just adequate for this application; therefore, it does produce hydrogen; however, it could be improved as discussed above with further development to achieve the performance that would be expected from a good active photocatalyst under visible light.

5 Conclusion

$MnCo_2O_4$ was successfully synthesized by Pechini and hydrothermal synthesis methods, obtaining the inverse spinel phase free of impurities. The synthesis process had a high impact on the material properties. The MCOP, calcined at 900°C, was the highest crystalline cobaltite synthesized (90%), sacrificing surface area and particle size (5 $m^2 \cdot g^{-1}$ and 500 nm), yet with a production of 9,200 nmol of H_2/g_{cat}. By synthesizing cobaltite by the hydrothermal method with NaOH, the surface area and particle size were improved (58 $m^2 \cdot g^{-1}$ and 40 nm) obtaining a production of 5,074 nmol of H_2/g_{cat}. Modifying this method, using acetates, urea, and EG as precursors, a significant increase in surface area (155 $m^2 \cdot g^{-1}$), a small particle size of 10 nm, and an improvement in performance were achieved, obtaining 12,050 nmol of H_2/g_{cat}, being the best performance at 8 h of the 3 MCOs synthesized by different synthesis methods.

Acknowledgments: First author is grateful for the support of the National Council of Science and Technology of Mexico (CONACYT) for the scholarship to complete a doctor´s degree at Centro de Investigación en Materiales Avanzados, S. C. (CIMAV). Authors greatly appreciate the help of Andrés Isaak González Jacquez, Luis Gerardo Silva Vidaurri, Luz Idalia Ibarra Rodriguez, Karla Campos Venegas, César Cutberto Leyva Porras, Claudia Alejandra Hernández Escobar, and Luis de la Torre Sáenz for their support in performing the XRD, XPS, STEM, PL, and BET analyses. Additionally, thanks to the National Nanotechnology Laboratory (NANOTECH) at CIMAV Chihuahua for their facilities to complete characterization tests.

Funding information: Authors state no funding involved.

Author contributions: Jaime A. Jiménez-Miramontes: conceptualization, investigation, methodology, formal analysis, writing – original draft, and writing – review & editing; Jorge L. Domínguez-Arvizu: investigation, conceptualization, formal analysis, and methodology; Felipe A. Gaxiola-Cebreros: investigation and conceptualization; Blanca C. Hernández-Majalca: investigation and conceptualization; Juan C. Pantoja-Espinoza: investigation, conceptualization, and formal analysis; Jesús M. Salinas-Gutiérrez: investigation, methodology, and resources; Alejandro López-Ortiz: conceptualization, writing – review & editing, and resources; Virginia Collins-Martínez: conceptualization, methodology, project administration, resources, formal analysis, supervision, writing – original draft, and writing – review & editing.

Conflict of interest: Authors state no conflict of interest.

References

[1] International Energy Agency. Energy Access Outlook 2017: From Poverty to Prosperity, 2017.
[2] Vozniuk, O., N. Tanchoux, J. M. Millet, S. Albonetti, F. Di Renzo, and F. Cavani. Spinel mixed oxides for chemical-loop reforming: from solid state to potential application. *Studies in surface science and catalysis*, 178, Elsevier B.V, 2019, pp. 281–302.
[3] Martin, D. J. *Investigation into high efficiency visible light photocatalysts for water reduction and oxidation*, Springer International Publishing, Switzerland, 2015.
[4] Li, R., and C. Li. *Photocatalytic water splitting on semiconductor-based photocatalysts*, Elsevier, B. V., Amsterdam, 2017, pp. 1–57.
[5] Armatas, G. S. *In new and future developments in catalysis*, Elsevier B.V, Amsterdam, 2013, pp. 305–332.

[6] Sarkar, J. and S. Bhattacharyya. Application of graphene and graphene-based materials in clean energy-related devices minghui. *Archives of Thermodynamics*, Vol. 33, No. 4, 2012, pp. 23–40.
[7] Xie, M. Y., K. Y. Su, X. Y. Peng, R. J. Wu, M. Chavali, and W. C. Chang. Hydrogen production by photocatalytic water-splitting on Pt-Doped TiO_2-ZnO under visible light. *Journal of the Taiwan Institute of Chemical Engineers*, Vol. 70, 2017, pp. 161–167.
[8] Martha, S., K. H. Reddy, K. M. Parida, and P. K. Satapathy. Enhanced photocatalytic activity over N-Doped GaZn mixed oxide under visible light irradiation. *International Journal of Hydrogen Energy*, Vol. 37, No. 1, 2012, pp. 115–124.
[9] Chen, W., H. Liu, X. Li, S. Liu, L. Gao, L. Mao, et al. Polymerizable complex synthesis of $SrTiO_3$:(Cr/Ta) photocatalysts to improve photocatalytic water splitting activity under visible light. *Applied Catalysis B: Environmental*, Vol. 192, 2016, pp. 145–151.
[10] Fang, W., S. Yao, L. Wang, and C. Li. Enhanced photocatalytic overall water splitting via hollow structure Pt/g-C_3N_4/BiOBr photocatalyst with S-scheme heterojunction. *Journal of Alloys and Compounds*, Vol. 891, 2022, id. 162081.
[11] Rosseler, O., M. V. Shankar, M. K. Du, L. Schmidlin, N. Keller, and V. Keller. Solar light photocatalytic hydrogen production from water over Pt and Au/TiO_2 (Anatase/Rutile) photocatalysts: influence of noble metal and porogen promotion. *Journal of Catalysis*, Vol. 269, No. 1, 2010, pp. 179–190.
[12] Selcuk, M. Z., M. S. Boroglu, and I. Boz. Hydrogen production by photocatalytic water-splitting using nitrogen and metal Co-Doped TiO_2 powder photocatalyst. *Reaction Kinetics, Mechanisms and Catalysis*, Vol. 106, No. 2, 2012, pp. 313–324.
[13] Sadat, N., S. Khameneh, and R. Mohammadpour. Band-gap narrowing and electrochemical properties in N-Doped and reduced anodic TiO_2 nanotube arrays. *Electrochimica Acta*, Vol. 270, 2018, pp. 245–255.
[14] Mao, L., H. Liu, S. Liu, Q. Ba, H. Wang, L. Gao, et al. Pt-Ru Bi-Metal Co-Catalyst: preparation, characterization and its effect on CdS's activity for water splitting under visible light. *Materials Research Bulletin*, Vol. 93, 2017, pp. 9–15.
[15] Chen, Z., P. Chen, P. Xing, X. Hu, H. Lin, L. Zhao, et al. Rapid fabrication of $KTa_{0.75}Nb_{0.25}$/g-C_3N_4 composite via microwave heating for efficient photocatalytic H2 evolution. *Fuel*, Vol. 241, 2019, pp. 1–11.
[16] Zhang, Q., P. Chen, L. Chen, M. Wu, X. Dai, P. Xing, et al. Facile fabrication of novel Ag_2S/K-g-C_3N_4 composite and its enhanced performance in photocatalytic H_2 evolution. *Journal of Colloid and Interface Science*, Vol. 568, 2020, pp. 117–129.
[17] Wang, D., X. Wang, J. Liu, M. Zhang, Y. Song, Z. Zhang, et al. Preparation of high proportion of Z-Scheme Er^{3+}:$Y_3Al_5O_{12}$@Nb_2O_5/Pt/In_2O_3 composite for enhanced visible-light driven photocatalytic hydrogen production. *Materials Science and Engineering B: Solid-State Materials for Advanced Technology*, Vol. 257, 2020, id. 114549.
[18] Lv, Z., P. Liu, Y. Zhao, C. Peng, X. Y. Meng, and Y. X. Pan. Visible-light-driven photocatalytic H_2 production from H_2O boosted by anchoring Pt and CdS Nanoparticles on a NaY Zeolite. *Chemical Engineering Science*, Vol. 255, 2022, id. 117658.
[19] Chen, D., H. Gao, Y. Yao, L. Zhu, X. Zhou, X. Peng, et al. Pd Loading, M^{n+} (n = 1, 2, 3) Metal Ions Doped TiO_2 nanosheets for enhanced photocatalytic H_2 production and reaction mechanism. *International Journal of Hydrogen Energy*, Vol. 47, No. 18, 2022, pp. 10250–10260.
[20] Zhao, Q., Z. Yan, C. Chen, and J. Chen. Spinels: controlled preparation, oxygen reduction/evolution reaction application, and beyond. *Chemical Reviews*, Vol. 117, No. 15, 2017, pp. 10121–10211.
[21] Ortega López, Y., H. Medina Vázquez, J. Salinas Gutiérrez, V. Guzmán Velderrain, A. López Ortiz, and V. Collins Martínez. Synthesis method effect of $CoFe_2O_4$ on its photocatalytic properties for H_2 production from water and visible light. *Journal of Nanomaterials*, Vol. 76, 2015, id. 985872.
[22] Domínguez-Arvizu, J. L., J. A. Jiménez-Miramontes, J. M. Salinas-Gutiérrez, M. J. Meléndez-Zaragoza, A. López-Ortiz, and V. Collins-Martínez. Study of $NiFe_2O_4$ nanoparticles optical properties by a six-flux radiation model towards the photocatalytic hydrogen production. *International Journal of Hydrogen Energy*, Vol. 44, No. 24, 2019, pp. 12455–12462.
[23] Jiménez-Miramontes, J. A., J. L. Domínguez-Arvizu, J. M. Salinas-Gutiérrez, M. J. Meléndez-Zaragoza, A. López-Ortiz, and V. Collins-Martínez. Synthesis, characterization and photocatalytic evaluation of strontium ferrites towards H_2 production by water splitting under visible light irradiation. *International Journal of Hydrogen Energy*, Vol. 42, No. 51, 2017, pp. 30257–30266.
[24] Mohanta, O., Y. N. Singhbabu, S. K. Giri, D. Dadhich, N. N. Das, and R. K. Sahu. Degradation of congo red pollutants using microwave derived $SrFe_{12}O_{19}$: an efficient magnetic photocatalyst under visible light. *Journal of Alloys and Compounds*, Vol. 564, 2013, pp. 78–83.
[25] Chen, D., F. Zhang, Q. Li, W. Wang, G. Qian, Y. Jin, et al. A promising synergistic effect of nickel ferrite loaded on the layered double hydroxide-derived carrier for enhanced photocatalytic hydrogen evolution. *International Journal of Hydrogen Energy*, Vol. 42, No. 2, 2017, pp. 867–875.
[26] Kim, H. G., P. H. Borse, J. S. Jang, E. D. Jeong, O. S. Jung, Y. J. Suh, et al. Fabrication of $CaFe_2O_4$/$MgFe_2O_4$ bulk heterojunction for enhanced visible light photocatalysis. *Chemical Communications*, Vol. 39, 2009, id. 5889.
[27] Dillert, R., D. H. Taffa, M. Wark, T. Bredow, and D. W. Bahnemann. Research update: photoelectrochemical water splitting and photocatalytic hydrogen production using ferrites (MFe_2O_4) under visible light irradiation. *APL Materials*, Vol. 3, No. 10, 2015, id. 104001.
[28] Li, C. J., J. N. Wang, X. Y. Li, and L. L. Zhang. Functionalization of electrospun magnetically separable TiO_2-Coated $SrFe_{12}O_{19}$ nanofibers: strongly effective photocatalyst and magnetic separation. *Journal of Materials Science*, Vol. 46, No. 7, 2011, pp. 2058–2063.
[29] Aziz, A. A., K. S. Yong, S. Ibrahim, and S. Pichiah. Enhanced magnetic separation and photocatalytic activity of nitrogen doped titania photocatalyst supported on strontium ferrite. *Journal of Hazardous Materials*, Vol. 199–200, 2012, pp. 143–150.
[30] Wu, Z., Y. Zhu, and X. Ji. $NiCo_2O_4$-based materials for electrochemical supercapacitors. *Journal of Materials Chemistry A*, Vol. 2, No. 36, 2014, pp. 14759–14772.
[31] Fang, L., Z. Jiang, H. Xu, L. Liu, Y. Guan, X. Gu, et al. Crystal-plane engineering of $NiCo_2O_4$ electrocatalysts towards efficient overall water splitting. *Journal of Catalysis*, Vol. 357, 2018, pp. 238–246.

[32] Gao, X., H. Zhang, Q. Li, X. Yu, Z. Hong, X. Zhang, et al. Hierarchical $NiCo_2O_4$ hollow microcuboids as bifunctional electrocatalysts for overall water-splitting. *Angewandte Chemie - International Edition*, Vol. 55, No. 21, 2016, pp. 6290–6294.

[33] Duan, L., F. Gao, L. Wang, S. Jin, and H. Wu. Hydrothermal synthesis and characterization of $MnCo_2O_4$ in the low-temperature hydrothermal process: their magnetism and electrochemical properties. *Journal of Advanced Ceramics*, Vol. 2, No. 3, 2013, pp. 266–273.

[34] Molin, S., P. Jasinski, L. Mikkelsen, W. Zhang, M. Chen, and P. V. Hendriksen. Low temperature processed $MnCo_2O_4$ and $MnCo_{1.8}Fe_{0.2}O_4$ as effective protective coatings for solid oxide fuel cell interconnects at 750°C. *Journal of Power Sources*, Vol. 336, 2016, pp. 408–418.

[35] Sharma, Y., N. Sharma, G. V. Subba Rao, and B. V. R. Chowdari. Studies on spinel cobaltites, $FeCo_2O_4$ and $MgCo_2O_4$ as anodes for Li-ion batteries. *Solid State Ionics*, Vol. 179, No. 15–16, 2008, pp. 587–597.

[36] Darbar, D., M. V. Reddy, S. Sundarrajan, R. Pattabiraman, S. Ramakrishna, and B. V. R. Chowdari. Anodic electrochemical performances of $MgCo_2O_4$ synthesized by oxalate decomposition method and electrospinning technique for Li-ion battery application. *Materials Research Bulletin*, Vol. 73, 2016, pp. 369–376.

[37] Liu, W. W., M. T. Jin, W. M. Shi, J. G. Deng, W. M. Lau, and Y. N. Zhang. First-principles studies on the structural stability of spinel $ZnCo_2O_4$ as an electrode material for lithium-ion batteries. *Scientific Reports*, Vol. 6, No. 1, 2016, id. 36717.

[38] Liu, J., Y. Xie, Y. Nan, G. Gou, X. Li, Y. Fang, et al. $ZnCo_2O_4$ nanoparticles derived from dual-metal-organic-frameworks embedded in multiwalled carbon nanotubes: a favorable electrocatalyst for the water splitting. *Electrochimica Acta*, Vol. 257, 2017, pp. 233–242.

[39] Shibli, S. M. A., P. S. Arun, and A. V. Raj. Exploration of octahedrally shaped $MnCo_2O_4$ catalyst particles for visible light driven photocatalytic water splitting reaction. *RSC Advances*, Vol. 5, No. 25, 2015, pp. 19393–19399.

[40] Zasada, F., J. Gryboś, P. Indyka, W. Piskorz, J. Kaczmarczyk, and Z. Sojka. Surface structure and morphology of $M[CoM']O_4$ (M = Mg, Zn, Fe, Co and M′ = Ni, Al, Mn, Co) spinel nanocrystals-DFT + U and TEM screening investigations. *Journal of Physical Chemistry C*, Vol. 118, No. 33, 2014, pp. 19085–19097.

[41] Kalubarme, R. S., H. S. Jadhav, D. T. Ngo, G. Park, J. G. Fisher, Y. Choi, et al. Simple synthesis of highly catalytic carbon-free $MnCo_2O_4$@Ni as an oxygen electrode for rechargeable Li–O_2 batteries with long-term stability. *Nature Publishing Group*, 2015, id. 13266.

[42] Xu, H., H. Shen, X. Song, X. Kong, Y. Zhang, and Z. Qin. Hydrothermal synthesis of porous hydrangea-like $MnCo_2O_4$ as anode materials for high performance lithium ion batteries. *Journal of Electroanalytical Chemistry*, Vol. 851, No. 3, 2019, id. 113455.

[43] Qi, J., P. Wang, Y. Yan, X. Zheng, J. Cao, and J. Feng. MCo_2O_4 (M = Co, Mn, Ni, Zn) nanosheet arrays constructed by two-dimension metal-organic frameworks as binder-free electrodes for lithium-ion batteries. *Vacuum*, Vol. 169, 2019, id. 108959.

[44] Li, Z., Y. Lv, Y. Yu, J. Yin, K. Song, B. Yang, et al. Fabrication of a three-dimensional interconnected mesoporous $MnCo_2O_4$ for rechargeable Li–O_2 batteries. *Journal of Alloys and Compounds*, Vol. 817, 2020, id. 152736.

[45] Song, K., L. Yuan, Z. Li, Y. Lv, B. Yang, Y. Yu, et al. Tuning $MnCo_2O_4$ nanowire arrays on carbon cloth as an efficient cathode catalyst for Li–O_2 batteries. *Electrochimica Acta*, Vol. 353, 2020, id. 136572.

[46] Merabet, L., K. Rida, and N. Boukmouche. Sol-gel synthesis, characterization, and supercapacitor applications of MCo_2O_4 (M = Ni, Mn, Cu, Zn) cobaltite spinels. *Ceramics International*, Vol. 44, No. 10, 2018, pp. 11265–11273.

[47] Dong, Y., Y. Wang, Y. Xu, C. Chen, Y. Wang, L. Jiao, et al. Facile synthesis of hierarchical nanocage $MnCo_2O_4$ for high performance supercapacitor. *Electrochimica Acta*, Vol. 225, 2017, pp. 39–46.

[48] Fan, L. Q., J. L. Huang, Y. L. Wang, C. L. Geng, S. J. Sun, Y. F. Huang, et al. High-capacity $MnCo_2O_4$ supported by reduced graphene oxide as an anode for lithium-ion capacitors. *Journal of Energy Storage*, Vol. 30, 2020, id. 101427.

[49] Borges, F. M. M., D. M. A. Melo, M. S. A. Câmara, A. E. Martinelli, J. M. Soares, J. H. de Araújo, et al. Magnetic behavior of nanocrystalline $MnCo_2O_4$ spinels. *Journal of Magnetism and Magnetic Materials*, Vol. 302, No. 2, 2006, pp. 273–277.

[50] Alqahtani, D. M., C. Zequine, C. K. Ranaweera, K. Siam, P. K. Kahol, T. Prasad, et al. Effect of metal ion substitution on electrochemical properties of cobalt oxide. *Journal of Alloys and Compounds*, Vol. 771, 2019, pp. 951–959.

[51] Zheng, J. and Z. Lei. Incorporation of CoO nanoparticles in 3D marigold flower-like hierarchical architecture $MnCo_2O_4$ for highly boosting solar light photo-oxidation and reduction ability. *Applied Catalysis B: Environmental*, Vol. 237, March, 2018, pp. 1–8.

[52] Olav, T., L. Sunde, T. Grande, and M. Einarsrud. Handbook of sol-gel science and technology. *Handbook of sol-gel science and technology*, Springer International Publishing, Switzerland, pp. 1–30.

[53] Byrappa, K. and M. Yoshimura. Hydrothermal technology–principles and applications. *Handbook of hydrothermal technology*, William Andrew Publishing, Norwich, NY, 2013, p. 893.

[54] Feng, S. H. and G. H. Li. Hydrothermal and solvothermal synthesis. In *Modern inorganic synthetic chemistry*, Elsevier B. V., Amsterdam, 2017, pp. 73–104.

[55] Li, J., O. Ridge, and J. Wu. Synthesis of nanoparticles via solvothermal and hydrothermal methods synthesis of nanoparticles via solvothermal and hydrothermal methods. *Handbook of nanoparticles*, Springer International Publishing, Switzerland, 2016, pp. 295–328.

[56] Domínguez-Arvizu, J. L., J. A. Jiménez-Miramontes, J. M. Salinas-Gutiérrez, M. J. Meléndez-Zaragoza, A. López-Ortiz, and V. Collins-Martínez. Optical properties determination of $NiFe_2O_4$ nanoparticles and their photocatalytic evaluation towards hydrogen production. *International Journal of Hydrogen Energy*, Vol. 42, No. 51, 2017, pp. 30242–30248.

[57] Li, D., F. Ruan, Y. Jin, Q. Ke, Y. Cao, H. Wang, et al. Design and synthesis of a highly efficient heterogeneous $MnCo_2O_4$ oxide catalyst for alcohol oxidation: DFT insight into the synergistic effect between oxygen deficiencies and bimetal species. *Catalysis Science and Technology*, Vol. 9, No. 2, 2019, pp. 418–424.

[58] Ge, X., Y. Liu, F. W. T. Goh, T. S. A. Hor, Y. Zong, P. Xiao, et al. Dual-phase spinel $MnCo_2O_4$ and spinel $MnCo_2O_4$/nanocarbon hybrids for electrocatalytic oxygen reduction and evolution. *ACS Applied Materials and Interfaces*, Vol. 615, 2014, pp. 12684–12691.
[59] Li, J., D. Xiong, L. Wang, M. K. S. Hirbod, and X. Li. High-performance self-assembly $MnCo_2O_4$ nanosheets for asymmetric supercapacitors. *Journal of Energy Chemistry*, Vol. 37, 2019, pp. 66–72.
[60] Kurajica, S., I. Minga, I. Grčić, V. Mandić, and M. Plodinec. The utilization of modified alkoxide as a precursor for solvothermal synthesis of nanocrystalline titania. *Materials Chemistry and Physics*, Vol. 196, 2017, pp. 194–204.
[61] Yoon, M. Y., E. J. Lee, R. H. Song, and H. J. Hwang. Preparation and properties of a $MnCo_2O_4$ for ceramic interconnect of solid oxide fuel cell via glycine nitrate process. *Metals and Materials International*, Vol. 17, No. 6, 2011, pp. 1039–1043.
[62] Lesani, P., A. Babaei, A. Ataie, and E. Mostafavi. Nanostructured $MnCo_2O_4$ synthesized via Co-precipitation method for SOFC interconnect application. *International Journal of Hydrogen Energy*, Vol. 41, No. 45, 2016, pp. 20640–20649.
[63] Stangeland, K., D. Yosef, Y. Ding, and Z. Yu. Mesoporous manganese-cobalt oxide spinel catalysts for CO_2 hydrogenation to methanol. *Journal of CO_2 Utilization*, Vol. 32, 2019, pp. 146–154.
[64] Rotaru, R., M. Savin, N. Tudorachi, C. Peptu, P. Samoila, L. Sacarescu, et al. Ferromagnetic iron oxide-cellulose nanocomposites prepared by ultrasonication. *Polymer Chemistry*, Vol. 9, No. 7, 2018, pp. 860–868.
[65] Bindu, P. and S. Thomas. Estimation of lattice strain in ZnO nanoparticles: x-ray peak profile analysis. *Journal of Theoretical and Applied Physics*, Vol. 8, No. 4, 2014, pp. 123–134.
[66] Wang, S., Y. Hou, and X. Wang. Development of a stable $MnCo_2O_4$ cocatalyst for photocatalytic CO_2 reduction with visible light. *ACS Applied Materials and Interfaces*, Vol. 7, No. 7, 2015, pp. 4327–4335.
[67] Fairley, N., V. Fernandez, M. Richard-Plouet, C. Guillot-Deudon, J. Walton, E. Smith, et al. systematic and collaborative approach to problem solving using x-ray photoelectron spectroscopy. *Applied Surface Science Advances*, Vol. 5, June, 2021, id. 100112.
[68] Liu, D., C. Zhang, Y. Yu, Y. Shi, Y. Yu, Z. Niu, et al. Hydrogen evolution activity enhancement by tuning the oxygen vacancies in self-supported mesoporous spinel oxide nanowire arrays. *Nano Research*, Vol. 11, No. 2, 2018, pp. 603–613.
[69] Jadhav, H. S., A. Roy, W. J. Chung, and J. G. Seo. Free standing growth of $MnCo_2O_4$ nanoflakes as an electrocatalyst for methanol electro-oxidation. *New Journal of Chemistry*, Vol. 41, No. 24, 2017, pp. 15058–15063.
[70] Wang, Z., D. Wang, Z. Lu, J. Liu, D. Xuan, Q. Liu, et al. Battery-type $MnCo_2O_4$@carbon nanofibers composites with mesoporous structure for high performance asymmetric supercapacitor. *Diamond and Related Materials*, Vol. 119, 2021, id. 108586.
[71] Krishnan, S. G., M. Harilal, A. Yar, B. L. Vijayan, J. O. Dennis, M. M. Yusoff, et al. Critical influence of reduced graphene oxide mediated binding of M (M = Mg, Mn) with co ions, chemical stability and charge storability enhancements of spinal-type hierarchical MCo_2O_4 nanostructures. *Electrochimica Acta*, Vol. 243, 2017, pp. 119–128.
[72] Aghavnian, T., J. B. Moussy, D. Stanescu, R. Belkhou, N. Jedrecy, H. Magnan, et al. Determination of the cation site distribution of the spinel in multiferroic $CoFe_2O_4/BaTiO_3$ layers by x-ray photoelectron spectroscopy. *Journal of Electron Spectroscopy and Related Phenomena*, Vol. 202, 2015, pp. 16–21.
[73] Rodríguez-Rodríguez, A. A., M. B. Moreno-Trejo, M. J. Meléndez-Zaragoza, V. Collins-Martínez, A. López-Ortiz, E. Martínez-Guerra, et al. Spinel-type ferrite nanoparticles: synthesis by the oil-in-water microemulsion reaction method and photocatalytic water-splitting evaluation. *International Journal of Hydrogen Energy*, Vol. 4, 2019, pp. 12421–12429.
[74] Brunauer, S., P. H. Emmett, and E. Teller. Adsorption of gases in multimolecular layers. *Journal of the American Chemical Society*, Vol. 60, No. 2, 1938, pp. 309–319.
[75] Thommes, M., K. Kaneko, A. V. Neimark, J. P. Olivier, F. Rodriguez-reinoso, J. Rouquerol, et al. Physisorption of gases, with special reference to the evaluation of surface area and pore size distribution (IUPAC technical report). *Pure and applied chemistry*, Vol. 87, No. 9–10, 2015, pp. 1051–1069.
[76] Yuan, C., J. Li, L. Hou, L. Yang, L. Shen, and X. Zhang. Facile template-free synthesis of ultralayered mesoporous nickel cobaltite nanowires towards high-performance electrochemical capacitors. *Journal of Materials Chemistry*, Vol. 22, No. 31, 2012, pp. 16084–16090.
[77] Amirzhanova, A., N. Akmanşen, I. Karakaya, and Ö. Dag. mesoporous $MnCo_2O_4$, $NiCo_2O_4$, and $ZnCo_2O_4$ thin-film electrodes as electrocatalysts for the oxygen evolution reaction in alkaline solutions. *ACS Applied Energy Materials*, Vol. 4, No. 3, 2021, pp. 2769–2785.
[78] Mou, Q., Z. Guo, Y. Chai, B. Liu, and C. Liu. Visible-light assisted production of hydrocarbon fuels from carbon dioxide using Cu_2O@$MnCo_2O_4$ heterojunction. *Colloids and Surfaces A: Physicochemical and Engineering Aspects*, Vol. 623, March, 2021, id. 126707.
[79] Padmanathan, N. and S. Selladurai. Mesoporous $MnCo_2O_4$ spinel oxide nanostructure synthesized by solvothermal technique for supercapacitor. *Ionics*, Vol. 20, No. 4, 2014, pp. 479–487.
[80] Pike Technologies. Diffuse reflectance – theory and applications. *Application note*, 2011, p. 2.
[81] Habibi, M. H. and P. Bagheri. Enhanced photo-catalytic degradation of naphthol blue black on nano-structure $MnCo_2O_4$: charge separation of the photo-generated electron–hole pair. *Journal of Materials Science: Materials in Electronics*, Vol. 28, No. 1, 2017, pp. 289–294.
[82] Uke, S. J., V. P. Akhare, S. P. Meshram, D. R. Bambole, D. S. Thakre, G. N. Chaudhari, et al. Fabrication of spherical nanocrystalline $MnCo_2O_4$ via sol-gel citrate route for supercapacitor. *International Journal of Current Engineering And Scientific Research*, Vol. 1, 2018, pp. 254–261.
[83] Tang, Z.R., B. Han, C. Han, Y. J. Xu. One dimensional CdS based materials for artificial photoredox reactions. *Journal of Materials Chemistry A*, Vol. 5, No. 6, 2017, pp. 2387–2410.
[84] Leonat, L., G. Sbârcea, and I. V. Brañzoi. Cyclic voltammetry for energy levels estimation of organic materials. *UPB Scientific*

Bulletin. Series B: Chemistry and Materials Science, Vol. 75, No. 3, 2013, pp. 111–118.

[85] Shafiee, A., M. M. Salleh, and M. Yahaya. Determination of HOMO and LUMO of [6,6]-Phenyl C61-Butyric Acid 3-Ethylthiophene ester and poly (3-Octyl-Thiophene-2, 5-Diyl) through voltametry characterization. *Sains Malaysiana*, Vol. 40, No. 2, 2011, pp. 173–176.

[86] Melskens, J., B. W. H. Van De Loo, B. Macco, L. E. Black, S. Smit, and W. M. M. Kessels. Passivating contacts for crystalline silicon solar cells: from concepts and materials to prospects. *IEEE Journal of Photovoltaics*, Vol. 8, No. 2, 2018, pp. 373–388.

[87] Bondarenko, A. S. and G. A. Ragoisha. Variable Mott-Schottky plots acquisition by potentiodynamic electrochemical impedance spectroscopy. *Journal of Solid State Electrochemistry*, Vol. 9, No. 12, 2005, pp. 845–849.

[88] Admassie, S., O. Inganäs, W. Mammo, E. Perzon, and M. R. Andersson. Electrochemical and optical studies of the band gaps of alternating polyfluorene copolymers. *Synthetic Metals*, Vol. 156, No. 7–8, 2006, pp. 614–623.

[89] Inamdar, S. N., P. P. Ingole, and S. K. Haram. Determination of band structure parameters and the quasi-particle gap of CdSe quantum dots by cyclic voltammetry. *ChemPhysChem*, Vol. 9, No. 17, 2008, pp. 2574–2579.

[90] Chwang, R., B. J. Smith, and C. R. Crowell. Contact size effects on the Van der Pauw method for resistivity and hall coefficient measurement. *Solid-State Electronics*, Vol. 17, No. 12, 1974, pp. 1217–1227.

[91] Ponmudi, S., R. Sivakumar, C. Sanjeeviraja, C. Gopalakrishnan, and K. Jeyadheepan. Facile fabrication of spinel structured N-Type $CuAl_2O_4$ thin film with nano-grass like morphology by sputtering technique. *Applied Surface Science*, Vol. 483, January, 2019, pp. 601–615.

[92] Selim, S., E. Pastor, M. Garc, M. R. Morris, L. Franca, M. Sachs, et al. Impact of oxygen vacancy occupancy on charge carrier dynamics in $BiVO_4$ photoanodes. *Journal of the American Chemical Society*, Vol. 141, No. 47, 2019, pp. 18791–18798.

[93] Son, S. Y., Y. Kim, J. Lee, G. Y. Lee, W. T. Park, Y. Y. Noh, et al. High-field-effect mobility of low-crystallinity conjugated polymers with localized aggregates. *Journal of the American Chemical Society*, Vol. 138, No. 26, 2016, pp. 8096–8103.

[94] Chen, P., L. Chen, S. Ge, W. Zhang, M. Wu, P. Xing, et al. Microwave heating preparation of phosphorus doped g-C_3N_4 and its enhanced performance for photocatalytic H_2 evolution in the help of Ag_3PO_4 nanoparticles. *International Journal of Hydrogen Energy*, Vol. 45, No. 28, 2020, pp. 14354–14367.

[95] Hen, X. S., P. R. Amvall, P. R. Iblet, and Y. A. Oyagi. Improvements of the optical and electrical properties of GaN films by using in-doping method during growth improvements of the optical and electrical properties of GaN films. *Japanese Journal of Applied Physics*, Vol. 38, No. 4B, 1999, pp. L411–L413.

[96] Chakroune, N., G. Viau, S. Ammar, N. Jouini, P. Gredin, M. J. Vaulay, et al. Synthesis, characterization and magnetic properties of disk-shaped particles of a cobalt alkoxide: $Co^{II}(C_2H_4O_2)$. *New Journal of Chemistry*, Vol. 29, No. 2, 2005, pp. 355–361.

[97] Ai, M., J. W. Zhang, Y. W. Wu, L. Pan, C. Shi, and J. J. Zou. Role of vacancies in photocatalysis: a review of recent progress. *Chemistry – An Asian Journal*, Vol. 15, No. 22, 2020, pp. 3599–3619.

[98] Zhang, S., W. Pu, A. Chen, Y. Xu, Y. Wang, C. Yang, et al. Oxygen vacancies enhanced photocatalytic activity towards VOCs oxidation over Pt deposited Bi_2WO_6 under visible light. *Journal of Hazardous Materials*, Vol. 384, 2020, id. 121478.